



# Representation of extreme El Niño events and associated atmospheric moisture flux divergence in the central-eastern tropical Pacific in a CMIP6 model ensemble

Janeet Sanabria<sup>a,b,\*</sup> , Raphael Neukom<sup>a,c,d</sup>, Alan Llacza<sup>e</sup>, Nadine Salzmann<sup>a,c,d</sup>, Pierluigi Calanca<sup>f</sup>

<sup>a</sup> Alpine Cryosphere and Geomorphology Group, Department of Geosciences, University of Fribourg, CH-1700, Fribourg, Switzerland

<sup>b</sup> Universidad Nacional Agraria la Molina, Facultad de Ciencias, Departamento de Física y Meteorología, Av. La Molina s/n, La Molina, Switzerland

<sup>c</sup> WSL Institute for Snow and Avalanche Research SLF, Flüelastr. 11, CH-7260, Davos Dorf, Switzerland

<sup>d</sup> Climate Change, Extremes, and Natural Hazards in Alpine Regions Research Center CERC, Flüelastr. 11, CH-7260, Davos Dorf, Switzerland

<sup>e</sup> Servicio Nacional de Meteorología e Hidrología, Lima Perú, Switzerland

<sup>f</sup> Agroscope, Switzerland

## ABSTRACT

Extreme El Niño events entail important socio-economic challenges, both in regions such as South America directly affected by their impacts and in regions around the world that are influenced by the associated teleconnections. Uncertainty remains about the ability of recent climate models to reproduce the characteristics and impacts of extreme El Niño events. In this study, we evaluate the ability of 32 CMIP6 models to simulate extreme El Niño events, focusing on their occurrence, their seasonal evolution, and the characteristics of the associated atmospheric moisture flux divergence. Our results reveal the reasonable performance of the CMIP6 ensemble in reproducing the observed anomalies and seasonal cycles of extreme El Niño events. The ensemble mean also captures the average temporal evolution and magnitudes of moisture flux anomalies, but fails to reproduce some important aspects of the associated spatial patterns. Most individual models have marked deficiencies in adequately simulating the seasonal cycle of atmospheric moisture flux divergence dynamics and reproducing a clear distinction between moderate and extreme events. The latter indicates that the atmospheric–ocean coupling and resulting precipitation anomaly patterns over Ecuador and northern Peru are still not correctly reproduced by the individual models. These deficiencies echo previous studies and underscore the limitations of current global climate models in providing reliable insights into the impacts of climate change on El Niño extremes and their consequences for regional atmospheric dynamics and precipitation. This work highlights the need for further research to improve model representations of extreme El Niño events and their associated impacts on vulnerable regions, thereby facilitating more effective risk management and adaptation measures.

## 1. Introduction

The El Niño–Southern Oscillation (ENSO)—the major ocean–atmosphere coupled mode of interannual climate variability (Bjerknes, 1969; Neelin et al., 1998; Battisti and Hirst, 1989)—is associated with large-scale atmospheric variability that affects weather and climate worldwide (Rasmusson and Carpenter, 1982; Ropelewski and Halpert, 1987; Kiladis and Diaz, 1989; Hoerling et al., 1997; Davey et al., 2014). In the tropics, ENSO affects the Walker circulation (Bjerknes, 1966, 1969) and reorders the hydrological cycle, with implications for the precipitation regime over the east-central tropical Pacific (Peixoto and Oort, 1992; Trenberth et al., 2002) and the globe (Capotondi and Coauthors, 2015; Kim et al., 2015). The positive sea surface temperature (SST) anomaly during El Niño, the warm phase of ENSO, favors

conditions for the initiation of atmospheric moisture convergence over the western tropical Pacific Ocean and propagation of the convergence belt eastward along the central-eastern Pacific (Wang, 2000; Paixao Veiga et al., 2005; Boers et al., 2014; Xu et al., 2015).

The dynamics of an El Niño event is controlled by the evolution of the SST anomaly (Chen and Jin, 2022) and spans 2–3 years. The growth phase starts during the boreal summer and autumn of the first year (Vimont et al., 2022) and ends toward the end of the year (Rasmusson and Carpenter, 1982; Wallace et al., 1998; Larkin and Harrison, 2002), followed by a rapid decay phase during boreal winter and spring of the following year (Lengaigne and Vecchi, 2010; Song et al., 2020).

El Niño events considerably differ in their intensity. The events that occurred in 1972/1973, 1982/1983, 1997/1998, and 2015/2016 stand out for their extreme magnitude and are therefore termed super (Hong

\* Corresponding author. Alpine Cryosphere and Geomorphology Group, Department of Geosciences, University of Fribourg, CH-1700, Fribourg, Switzerland  
E-mail address: [jsanabria@lamolina.edu.pe](mailto:jsanabria@lamolina.edu.pe) (J. Sanabria).

<https://doi.org/10.1016/j.wace.2025.100746>

Received 6 November 2023; Received in revised form 31 January 2025; Accepted 7 February 2025

Available online 8 February 2025

2212-0947/© 2025 The Authors. Published by Elsevier B.V. This is an open access article under the CC BY license (<http://creativecommons.org/licenses/by/4.0/>).

et al., 2014; Hameed et al., 2018) or extreme (Sanabria et al., 2018; Hameed et al., 2018; Dewitte and Takahashi, 2019) El Niño events. They were characterized by comparably large amplitudes in the Niño 3.4 region (central to eastern equatorial Pacific: 5°S to 5°N, 170°W to 120°W), strong eastern-Pacific warming, strong atmospheric coupling (Santoso et al., 2017; Chen et al., 2017; Dewitte and Takahashi, 2019), and distinct patterns of the atmospheric moisture flux divergence (Xu et al., 2015). These conditions caused heavy rainfall along the western Pacific slopes of the Tropical Andes (Sanabria et al., 2018, 2019; Thielen et al., 2023), but rainfall deficits along the Amazonian side of the Andes in southern Peru (Sulca et al., 2018; Sanabria et al., 2019; Humane-s-Fuente et al., 2020). Anomalous rainfall conditions entailed by these extreme El Niño events were also observed in other South American regions but with specificities depending on the event (Cai et al., 2020).

The ability to simulate El Niño extremes is of great socio-economic importance, particularly in South American countries that are directly exposed to anomalous ENSO dynamics (Cai et al., 2020), but more generally in countries around the world influenced by global El Niño teleconnections (e.g., King et al., 2020; McKenna et al., 2020). In Peru, for instance, the Pacific watershed is home to 30% of the country's population, major agro-industries producing goods for export, and important water reservoirs. On the other side of the country, the Amazon watershed provides livelihood for most residents of the area via food security crops, hydroelectric dams, and mining. Therefore, any change in the meteorological impacts of extreme El Niño events in these two core areas of Peru can have severe economic impacts.

Given the implications of extreme El Niño events for South American countries and globally, there is much interest in understanding how global warming can affect their occurrence and properties. Uncertainties in current projections of ENSO response to global warming (Latif and Keenlyside, 2009) are considerable, and ultimately, the possibility of developing future scenarios for extreme El Niño events depends on the ability of global climate models (GCMs) to capture their essential features. Some studies have found that tropical Pacific seasonality (Hou and Tang, 2022) and ENSO teleconnections (Planton et al., 2021) are simulated in a satisfactory manner in coupled global climate models. With respect to the GCMs participating in the various phases of the Coupled Model Intercomparison Project (CMIP), Hou and Tang (2022), Liao et al., 2021, and Chen et al. (2017) found deficiencies in relation to the representation of the 4–7 year periodicity of the ENSO, the strength of El Niño and La Niña events, and the seasonal evolution of these events. Progress in the simulation of ENSO has nevertheless been seen during the fifth evaluation phase (CMIP5) (e.g., Guilyardi et al., 2012) as well as during the sixth evaluation phase (CMIP6) (Hou and Tang, 2022; Planton et al., 2021). Whether the models participating in CMIP6 are better than their predecessors that participated in CMIP 5 remains an open question (De Silva et al., 2023).

The overarching aim of this study is to assess the ability of the CMIP6 model ensemble (32 members) to reproduce the observed characteristics of extreme El Niño events in both the oceanic and atmospheric domains. We analyze the magnitude, seasonal cycle and spatial patterns of extreme El Niño events and compare these characteristics with moderate events. We begin by determining statistical thresholds for the separation of extreme and moderate El Niño events based on the relative Niño-3.4 index (herein denoted as *rENSOi*). The *rENSOi* was introduced by van Oldenborgh et al. (2021) to overcome the sensitivity of other indices commonly used to track the evolution of the ENSO phenomenon (Trenberth, 2020) with respect to global warming. Given the robustness of the index, we consider the detection of extreme El Niño events based on the *rENSOi* an interesting alternative to the calculation of the EOF modes from monthly SST anomalies (Takahashi et al., 2011) or the classification of El Niño events based on boreal winter rainfall in the Niño 3 region (Cai et al., 2014, 2015).

We then examine the ability of the models to reproduce the gap between the joint probability densities of the peaks of the *rENSOi* and the divergence of the atmospheric moisture flux during both extreme

and moderate events. Further, we assess the magnitude and seasonal cycle of extreme El Niño events by contrasting the time series of the *rENSOi* and the moisture flux divergence over the tropical Pacific as simulated by the selected 32 CMIP6 models by comparison with the observational benchmark.

Finally, we examine the ability of the selected GCMs to reproduce the spatio-temporal properties of the atmospheric moisture flux divergence over the central-eastern tropical Pacific during the detected extreme El Niño events. We consider the moisture flux divergence to be a measure of the atmospheric coupling with SST and a precursor of anomalous precipitation over Ecuador and northern Peru. To assess the capacity of the CMIP6 ensemble to capture the specific characteristics of extreme El Niño events, the properties of the events are further compared to moderate El Niño events in models and observations.

## 2. Data and methods

### 2.1. Monthly fields from HadISST, ERA5 and CMIP6

We obtained monthly sea-surface temperature (SST) observations spanning the years 1901–2019 from the Met Office Hadley Centre's sea ice and sea-surface temperature dataset (HadISST) (Rayner et al., 2003). The data have a spatial resolution of 1° × 1°. To estimate the atmospheric moisture flux divergence, we employed monthly fields of vertically integrated eastward and northward water vapor fluxes covering the period 1950 to 2019. The data were extracted from the fifth generation European Centre for Medium-Range Weather Forecasts (ECMWF) reanalysis for the global climate and weather (ERA5) (Bell et al., 2021), as available in the Copernicus Climate Change Service (C3S) data repository (C3S, 2017). The data are provided on a longitude/latitude grid with a spatial resolution of 0.5° × 0.5° and 19 pressure levels with a vertical coverage ranging from 1 000 hPa to 1 hPa.

With respect to CMIP6, SST, wind and specific humidity data were extracted from the Earth System Grid Federation (ESGF) CMIP6 repository (Balaji et al., 2018), which was accessed from the following URL: <https://esgf-node.ipsl.upmc.fr/projects/cmip6-ipsl/>. The data are from the first realization of the historical simulation (r1i1p1) (Eyring et al., 2016). We used all models with 19 vertical pressure levels available from the surface to 0.01 hPa to be able to consistently calculate the vertically integrated moisture flux. This results in a total of 32 GCMs (Table 1), including those with good overall performance in atmospheric moisture balance (Watterson et al., 2021).

### 2.2. Relative Niño-3.4 index (*rENSOi*)

The *rENSOi* was introduced by van Oldenborgh et al. (2021) to monitor the evolution of the El Niño-Southern Oscillation while avoiding sensitivity to global warming. It is defined as the difference between the Niño 3.4 SST anomaly (5°N–5°S, 120°W–170°W; cf. Fig. 1) and the SST anomaly over all tropical oceans (20° S–20° N). The *rENSOi* is well suited to describe the influence of SST on large-scale atmosphere circulation, particularly the upper-tropospheric temperature, and provides a robust view of ENSO teleconnections (Oldenborgh et al., 2021; Johnson and Kosaka, 2016). In addition, *rENSOi* has the advantage of being less sensitive with respect to biases in the SST fields compared to other ENSO indices, such as Niño 3.4, NOAA-ONI, or the E and C index (van Oldenborgh et al., 2021). The *rENSOi* is also well suited for real-time monitoring and forecasting, and its strength in this respect has recently been confirmed by the analysis of L'Heureux et al. (2024).

We computed a reference time series of *rENSOi* using the HadISST monthly fields. In addition, we evaluated the *rENSOi* for all 32 CMIP6 models included in our study using the corresponding monthly SST fields.

**Table 1**

CMIP6 Models used in this study. In addition to the model names and institutions, the table provides information about the horizontal resolution of the oceanic and atmospheric components of the models, and the number of vertical atmospheric levels.

Model	Institution	Atmospheric grid	Oceanic grid	Pressure Levels
		(lat. x lon. in degrees)		
ACCESS-CM2	CSIRO-ARCCSS, Australia	1.25° × 1.875°	1° × 1°	19
ACCESS-ESM1-5	CSIRO, Australia	1.25° × 1.875°	1° × 1°	19
AWI-CM-1-1-MR	AWI, Germany	0.9° × 0.9°	0.938° × 0.938°	19
BCC-CSM2-MR	BCC, China	1.1° × 1.1°	1° × 1°	19
CAMS-CSM1-0	CAMS, China	1.1° × 1.1°	1° × 1°	19
CanESM5	Canadian Centre for Climate Modelling and Analysis, Canada	2.8° × 2.8°	1° × 1°	19
CESM2	NCAR, USA	0.94° × 1.25°	1° × 1°	19
CESM2-WACCM	NCAR, USA	0.94° × 1.25°	1° × 1°	19
CIESM	Tsinghua University, China	1° × 1°	0.9° × 1.3°	19
CMCC-ESM2	CMCC, Italy	1.9° × 2.8°	0.9° × 1.25°	19
CNRM-CM6-1-HR	CNRM, France	0.5° × 0.5°		19
CNRM-CM6-1	CNRM, France	1.4° × 1.4°	1° × 1°	19
CNRM-ESM2-1	CNRM, France	1° × 1°	1° × 1°	19
EC-Earth3-CC	EC-EARTH consortium/Europe	1° × 1°	1° × 1°	19
FGOALS-f3-L	Chinese Academy of Sciences/China	1° × 1°	1° × 1.3°	19
FIO-ESM-2-0	FIO QLN, China	0.27°-0.54° × 1.1°	1.25° × 0.9°	19
GFDL-CM4	GFDL, USA	1° × 1.25°	0.25° × 0.25°	19
GFDL-ESM4	GFDL, USA	1° × 1.25°	0.5° × 0.5°	19
GISS-E2-1-G	GISS, New York, USA	1.25° × 1°	1.25° × 1°	19
HadGEM3-GC31-LL	MOHC NERC, Hadley Centre, UK	1.25° × 1.875°	1° × 1°	19
HadGEM3-GC31-MM	MOHC, Hadley Centre, UK	0.55° × 0.83°	0.25° × 0.25°	19
IITM-ESM	CCCR-IITM, Indian	0.5° × 0.1°	1.875° × 1.9°	19
INM-CM5-0	INM, Rusia	1.5° × 2°	0.5° × 0.25°	19
IPSL-CM6A-LR	IPSL, France	1.3° × 2.5°	1° × 1°	19
MCM-UA-1-0	University of Arizona, USA	2° × 2°	2° × 2°	19
MIROC-ES2L	MIROC, Japan	2.8° × 2.8°	1° × 1°	19
MIROC6	CCSR, Japan	1.4° × 1.4°	1° × 1°	19
MPI-ESM1-2-HR	MPI, Germany	0.9375° × 0.9375°	0.4° × 0.4°	19
MRI-ESM2-0	MRI, Japan	1.125° × 1.125°	1.0° × 0.5°	19
NESM3	Naijing, University of information Science and Technology/China	1.9° × 1.9°	1° × 1°	19
NorESM2-MM	Norwegian Climate Centre, Norway	1.9° × 2.5°	1° × 1°	19
UKESM1-0-LL	Earth System Model, United Kingdom	1.25° × 1.875°	1° × 1°	19

### 2.3. Detection of extreme and moderate El Niño events

It has become common practice to classify El Niño events either through the use of leading EOFs modes of the SST in the tropical Pacific (Takahashi et al., 2011), or with regard to the average rainfall (5 mm d<sup>-1</sup>) during the months of December through February in the Niño 3 region (Cai et al., 2014, 2015). Although attractive for its simplicity, the use of absolute thresholds in connection with the evaluation of climate model results is problematic because it assumes that the model outputs are unbiased. This is normally not the case. To illustrate this problem, we show boxplots of the atmospheric moisture flux divergence (mean for DJF) from ERA5 and the 32 CMIP6 models (Fig. 2). The modeled distributions depart considerably from the observed distributions and differ from each other, especially over the negative divergence (i.e., convergence) values of interest for the characterization of extreme El Niño events. The use of a divergence threshold of -2 mm d<sup>-1</sup> analogous to the 5 mm d<sup>-1</sup> used by Cai et al. (2014, 2015) for precipitation, would allow for identifying the extreme events of 1982/1983, 1997/1998 and 2015/2016 (Fig. 3). However, application of this threshold to the time series of the spatially integrated divergence from CMIP6 would lead to an erroneous number of extreme events for many of the models, from zero in five models to more than ten extreme El Niño events in nine other models.

For this reason, we opted for a statistical definition of extreme El Niño events based on a percentile threshold for the rENSOi, which is directly applicable to instrumental records and GCM outputs without bias correction. The detection procedure involves the following steps: (a) divide the rENSOi time series into consecutive 12-month periods spanning October to September (of the following calendar year); (b) for each 12-month period, evaluate the maximum or peak value of the rENSOi (the peak is usually attained between November and February); (c) determine the percentile that elects the known extreme events in the instrumental record (Sanabria et al., 2018; Hameed et al., 2018; Dewitte and Takahashi, 2019), that is, 1972/1973, 1982/1983, 1997/1998 (if the HadISST time series is truncated in 2014 for the sake of consistency with the time range of the CMIP6 ensemble), and 2015/2016; and (d) use this same percentile to single out extreme El Niño events in the rENSOi time series from CMIP6.

This analysis of the observational rENSOi series suggested that extreme El Niño events are those that exceeded the 98th percentile. Accordingly, to identify extreme El Niño events in the CMIP6 models, we selected those events from each individual simulation that exceed the 98th percentile of the simulation's rENSOi time series. As the rENSOi records from CMIP6 consist of 114 entries (years), this implies that two to three events per record are identified per model. A similar procedure was applied to detect moderate El Niño events. Based on the literature, we decided to define moderate events as those classified as Central-Pacific (CP) by Yu and Kim (2013). We then determined the percentiles that would single out the same events in the historical series of the rENSOi (which were ultimately the 60th and 80th percentiles) and applied them to determine moderate events in the CMIP6 records.

### 2.4. Atmospheric moisture flux divergence

We evaluated the atmospheric moisture flux divergence,  $\nabla \cdot \vec{Q}$ , as:

$$\nabla \cdot \vec{Q} \equiv \nabla \cdot \left( \int_{1000 \text{ hPa}}^{1 \text{ hPa}} \vec{v} q \frac{dp}{g} \right) \quad (1)$$

where  $q$  is the specific humidity,  $\vec{v} = (u, v)$  the (horizontal) wind vector on a pressure surface,  $g$  is the acceleration due to gravity, and  $p$  denotes atmospheric pressure. The divergence of the vertically integrated moisture flux is a good proxy for the difference between evaporation and precipitation at the surface,  $E - P$ , because for a column extending in the vertical from the surface to the top of the atmosphere the water balance

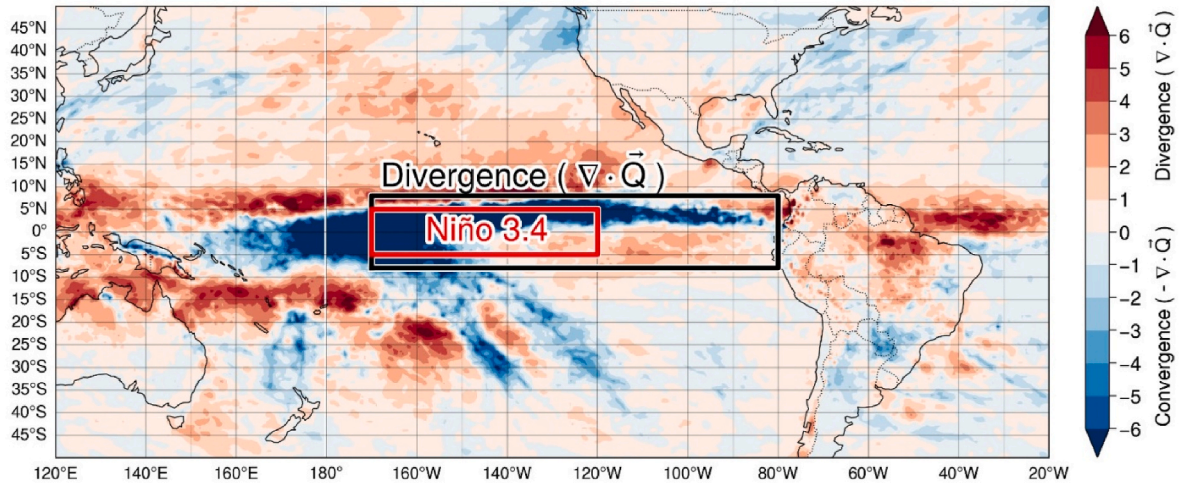


Fig. 1. Geographic map of the study region showing the Niño 3.4 region (red rectangle), as well as the region used to calculate the integrated Atmospheric moisture flux divergence (blue rectangle). The background field shows the ERA 5 moisture flux divergence field during DJF averaged over the period 2015–2016.

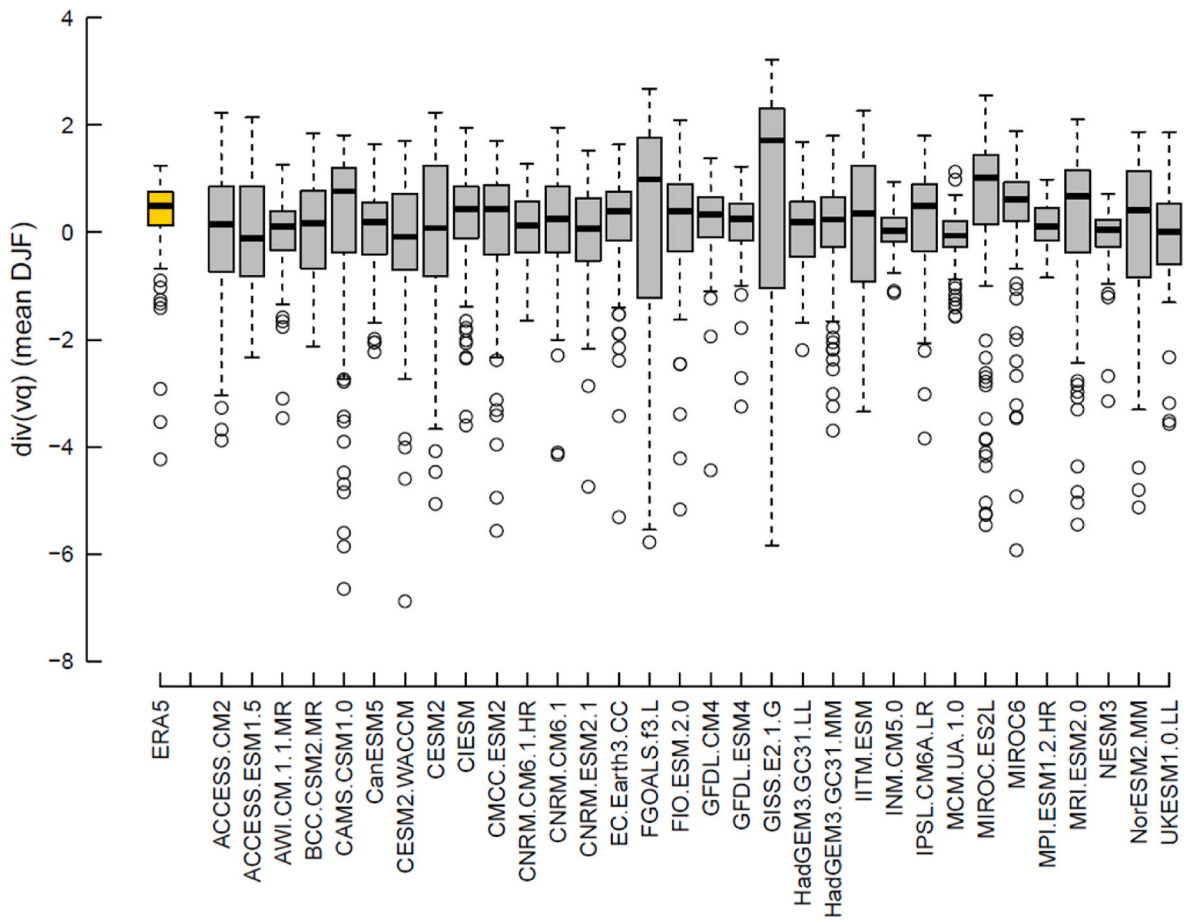


Fig. 2. Distribution of the spatially integrated, DJF-mean moisture flux divergence (area of integration as shown in Fig. 1) in the observations (ERA5, boxplot on the left in gold) and the 32 CMIP6 models (gray boxplots) over the available years.

equation reads:

$$\frac{\partial}{\partial t} W + \nabla \bullet \vec{Q} \approx \nabla \bullet \vec{Q} \equiv E - P \quad (2)$$

where  $\partial W/\partial t$  is the rate of change of precipitable water, a term that can be neglected if the time scales considered are long (monthly or longer).

The divergence,  $\nabla \bullet \vec{Q}$ , was initially evaluated on a grid-point basis (ERA5 or model grid). However, in order to relate the moisture flux divergence to rENSO, a spatially integral index, we integrated  $\nabla \bullet \vec{Q}$  over the central-eastern tropical Pacific area that extends from 170°W to 80°W in longitude and from 8°N to 8°S in latitude (Fig. 1). This area exhibits active temperature changes and is warmer than average, which

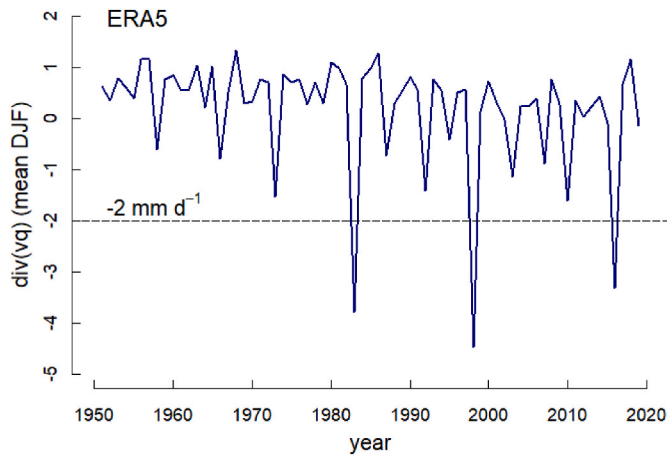


**Fig. 3.** Evolution of the spatially integrated monthly moisture flux divergence (area of integration as shown in Fig. 1) as evaluated based on ERA5, covering 1950–2019. The horizontal dashed line indicates a possible threshold for detecting extreme El Niño events (1982/1983, 1997/1998 and 2015/2016).

give rise to convective processes during extreme El Niño.

### 2.5. Evaluation of model performance

To evaluate the performance of the models with regard to the seasonal evolution of El Niño extremes, we analyzed the time series  $rENSO_i$  and  $\nabla \cdot \vec{Q}$  aligned over a 24-month period starting in January prior to the DJF season identified as peak year (e.g., January 1972 to December 1973 for the 1972/1973 extreme event). First, the 24-month time series of all extreme events in each dataset (observations and models) were averaged to assess the general characteristics of the evolution of extreme El Niño events. For each model simulation the correlation with observations, the root mean square difference (RMSD) and the standard deviation were calculated and plotted in a Taylor diagram. Second, we calculated a range of measures to assess the performance of the models as an ensemble. These measures include the timing of peak value within the 24-month cycle, the amplitude of the peak averaged across all extreme events, the range of the peak values across all extreme events, the number of months in which the average time series across all extreme events is outside the range of moderate events, and the difference between extreme and moderate events with respect to the average peak value of either the  $rENSO_i$  or the moisture flux divergence.

## 3. Results

### 3.1. Occurrence of extreme El Niño events

As shown in Fig. S1 (top left), the four extreme El Niño events single out in the observational time series of  $rENSO_i$  were, by construction, 1972/1973, 1982/1983, 1997/1998, and 2015/2016. All four events occurred in the second half of the historical record (1901–2019), and all of them were found to reach their maximum magnitude from November to January of the following year (cf. Table 2 and Fig. 5a, later). The extreme events were also striking in terms of moisture flux divergence (Fig. S1, top right), with average values around  $-4 \text{ mm d}^{-1}$  compared to an average of  $-1 \text{ mm d}^{-1}$  for the moderate events.

Concerning the occurrence of extreme El Niño events in CMIP6, Fig. S1 shows that, contrary to the observational data, not all of the two to three detected extreme El Niño events occurred during the second half of the investigated time span. Rather they were distributed across the entire period (cf. also Table 2). In this context it is important to stress that the years in the model outputs do not necessarily correspond to true calendar years, because the model runs, once started, are unconstrained

**Table 2**

Identified extreme El Niño events in the observational dataset (HadISST and ERA5; boldface) and the output of the 32 selected CMIP6 models, and month of the peak relative ENSO index, and the minimum aggregated moisture flux divergence, respectively. Both peak months refer to the 24-month interval of the El Niño cycle. Month 1 corresponds to January of the first year and month 13 corresponds to January of the second year and so on.

Dataset	Extreme El Niño events (start/end year)	Total number of extreme events	Peak month of the relative ENSO index	Peak month of the atmospheric moisture flux divergence
<b>HadISST</b>	<b>1972/1973,</b>	<b>4</b>	<b>12, 13, 13,</b>	<b>13, 13, 13, 12</b>
<b>ERA5</b>	<b>1982/1983,</b>		<b>11</b>	
	<b>1997/1998,</b>			
	<b>2015/2016</b>			
ACCESS-CM2	1972/1973, 1985/1986, 2011/2012	3	12, 10, 11	12, 12, 12
ACCESS-ESM1-5	1923/1924, 1972/1973, 2001/2002	3	13, 16, 13	10, 17, 2
AWI-CM1-1-MR	1910/1911, 1923/1924, 1969/1970	3	1,3 12, 13	14, 11, 12
BCC-CSM2-MR	1932/1933, 1943/1944	2	9, 10	11, 11
CAMS-CSM1-0	1945/1946, 1953/1954	2	10, 10	14, 11
CanESM5	1948/1949, 1973/1974, 2009/2010	3	11, 12, 14	12, 12, 16
CESM2-WACCM	1903/1904, 1935/1936	2	12, 11	13, 13
CESM2	1910/1911, 1934/1935, 1945/1946	3	12, 12, 12	12, 13, 14
CIESM	1960/1961, 1976/1977, 1990/1991	3	14, 12, 11	14, 13, 13
CMCC-ESM2	1912/1913, 1931/1932	2	11, 10	12, 12
CNRM-CM6-1-HR	1919/1920, 1928/1929, 2009/2010	3	12, 13, 12	12, 17, 13
CNRM-CM6-1	1957/1958, 2000/2001	2	12, 12	14, 13
CNRM-ESM2-1	1903/1904, 1937/1938, 1954/1955	3	12, 12,12	13, 3, 14
EC-Earth3-CC	1910/1911, 1982/1983, 1988/1989	3	12, 12, 13	13, 15,15
FGOALS-f3-L	1925/1926, 1939/1940, 2004/2005	3	9, 10, 10	8, 1,3 14
FIO-ESM2-0	1960/1961, 2000/2001	2	12, 11	13, 13
GFDL-CM4	1948/1949, 1970/1971, 1986/1987	3	11, 11, 11	12, 13, 14
GFDL-ESM4	1981/1982, 2012/2013	2	11, 12	12, 14
GISS-E2-1-G	1946/1947, 1960/1961, 2001/2002	3	8, 9, 9	1,2 13, 12
HadGEM3-GC31-LL	1923/1924, 1940/1941	2	12, 8	15, 7
HadGEM3-GC31-MM	1917/1918, 1924/1925	2	12, 11	13, 12
IITM-ESM	1931/1932, 1940/1941	2	10, 11	15, 15
INM-CM5-0	1946/1947, 1983/1984, 2002/2004	3	8, 9, 13	6, 8, 15

(continued on next page)

Table 2 (continued)

Dataset	Extreme El Niño events (start/end year)	Total number of extreme events	Peak month of the relative ENSO index	Peak month of the atmospheric moisture flux divergence
IPSL-CM6A-LR	1988/1989, 2009/2010	2	12, 12	15, 12
MCM-UA-1-0	1922/1923, 1998/1999	2	11, 9	11, 8
MIROC-ES2L	1911/1912, 1990/1991, 2004/2005	3	13, 1, 2 12	15, 13, 13
MIROC6	1962/1963, 2008/2009	2	11, 10	14, 12
MPI-ESM1-2-HR	1935/1936, 1985/1986, 2000/2001	3	17, 14, 17	17, 17 17
MRI-ESM2-0	1922/1923, 1954/1955, 2000/2001	3	11, 16, 13	12, 15, 14
NESM3	1934/1935, 1964/1965	2	12, 11	15, 12
NorESM2-MM	1962/1963, 2008/2009	2	11, 12	13, 14
UKESM1-0-LL	1929/1930, 1935/1936, 1965/1966	3	13, 12, 12	16, 13, 12

by observations. One model, MIROC-ES2L, further highlighted an extremely regular ENSO cycle, without an indication that extreme El Niño events would differ significantly from other El Niño events in terms of the rENSOi. For many of the models, extreme El Niño events were also clearly distinct from the moderate events with respect to the moisture

flux divergence (more than  $-2 \text{ mm d}^{-1}$  lower). Some models show a reduced difference between extreme and moderate  $\nabla \bullet \vec{Q}$  events, which mostly corresponds to a reduced difference between extreme and moderate rENSOi. In a few models, there was no clear difference at all between extreme and moderate events as for the divergence.

There was also considerable variability concerning the timing of the peak value (maximum magnitude) of the extreme El Niño events (Table 2). Some models simulated this timing up to six months earlier (BCC-CSM2-MR, CAMS-CSM1-0, FGOALS-f3-L, GISS-E2-1-G, HadGEM3-GC31-LL, INM-CM5-0, MCM-UA-1-0 and MIROC6) or later (ACCESS-ESM1-5, CanESM5, CIESM, MPI-ESM1-2-HR, MRI-ESM2-0 and UKESM1-0-LL) than in the observational data (November to January).

As revealed by Fig. S1, the peak value of observed atmospheric moisture flux divergence during extreme El Niño events, occurred, on average, 0 or 1 months after the oceanic peak. In CMIP6, the timing of the  $\nabla \bullet \vec{Q}$  peaks also show considerable variability. Some models simulated it up to five months earlier (ACCESS-ESM1-5, FGOALS-f3-L, HadGEM3-GC31-LL, INM-CM5-0, and MCM-UA-1-0) or four months after the observed peak (ACCESS-ESM1-5, CanESM5, CNRM-CM6-1-HR, EC-Earth3-CC, HadGEM3-GC31-LL, IITM-ESM, INM-CM5-0, IPSL-CM6A-LR, MIROC-ES2L, MPI-ESM1-2-HR, MRI-ESM2-0, NESM3, and UKESM1-0-LL; Table 2).

### 3.2. Overall performance of the CMIP6 models

For a general impression of the performance of the CMIP6 models with respect to the representation of extreme El Niño events, Taylor diagrams are presented in Fig. 4 for both the oceanic and the atmospheric components. The diagrams report statistics computed by comparing the mean evolution of extreme El Niño events over a 24-month period (average evolution over all events) in the observations

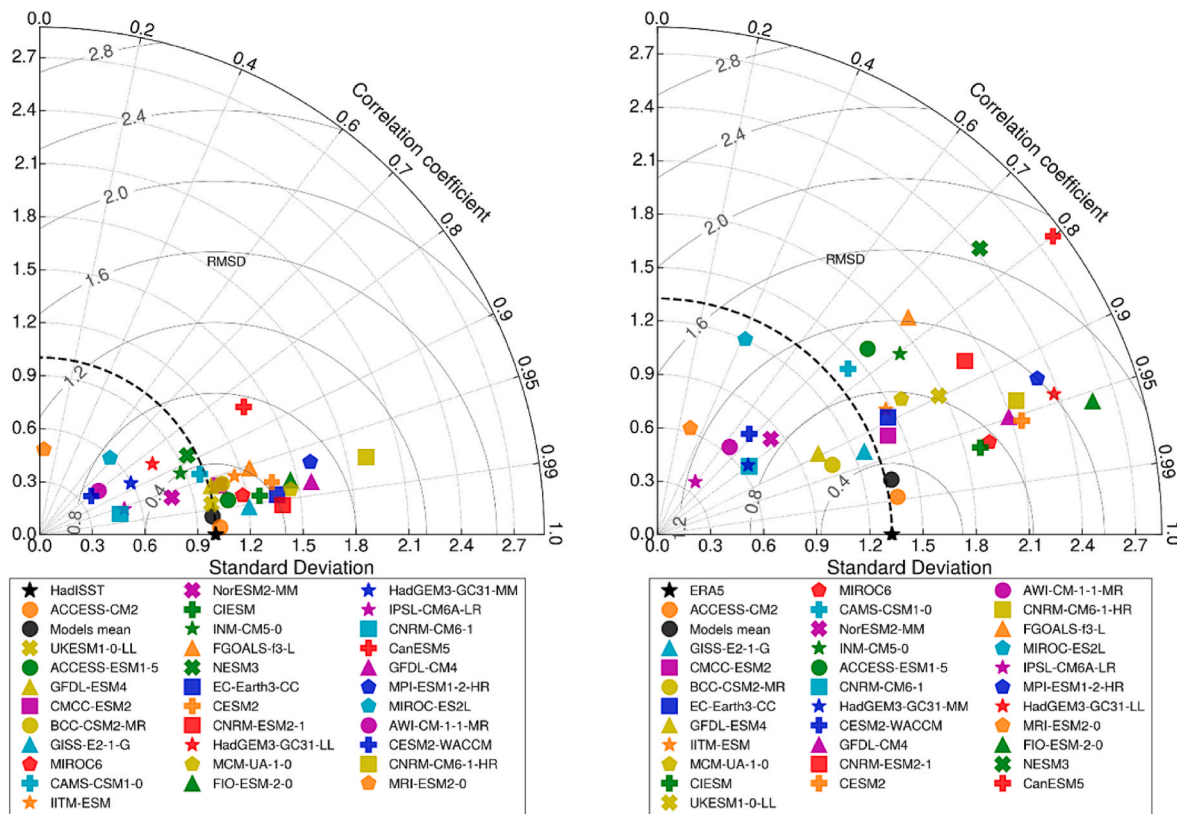
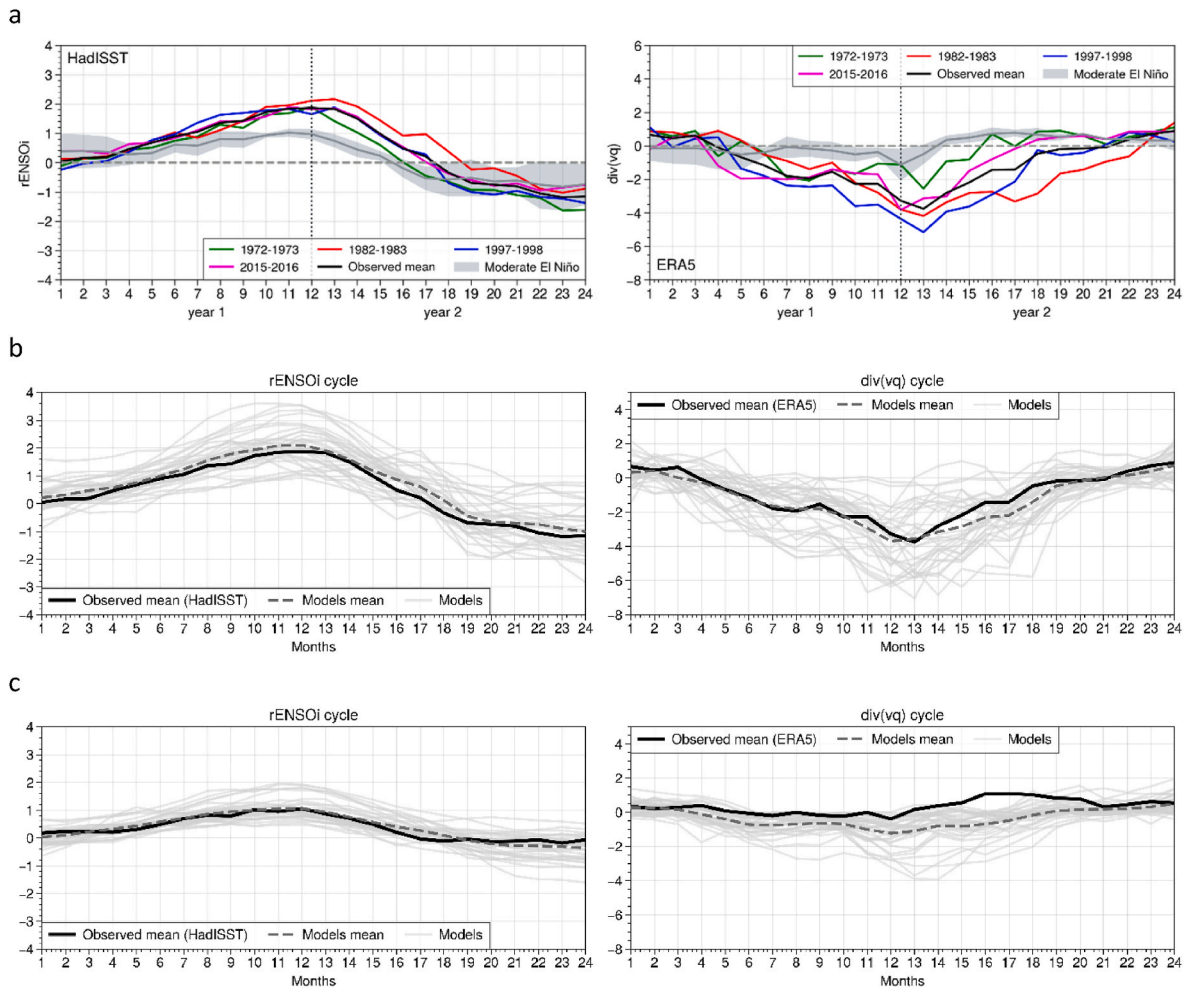


Fig. 4. Taylor diagrams showing the correlation between observations and models, the standard deviation and the root mean square difference (RMSD) between observations and models. Values are shown for the average 24-month time series across all extreme El Niño events for each dataset. a) relative ENSO index (rENSOi). b) Moisture flux divergence. The black filled circle shows the multi-model mean.



**Fig. 5.** Evolution of the relative ENSO index (left) and moisture flux divergence (right) over a 2-year period. a) Cycle of the observed extreme El Niño events (HadISST: left; ERA5: right) illustrated by the colored curves. The gray shaded area shows the mean  $\pm 1$  standard deviation of all moderate El Niño events. b) Cycle of the extreme El Niño events of the individual CMIP6 models illustrated by continuous gray lines. Dashed black lines: mean of all models; black solid line: mean of the observations. c) As b) but for the moderate events.

and the individual models. Specifically, the Taylor diagrams display correlation with the observed values, RMSD between observed and simulated values, and standard deviation of the  $rENSO_i$  (Fig. 4a) and  $\nabla \bullet \vec{Q}$  (Fig. 4b).

Correlations were relatively high for most models, with 24 out of the 32 simulations showing a value above 0.9. Similarly, RMSD was below 0.4 for 16 models, indicating that, on average, the simulated extreme events followed the observed temporal SST evolution comparatively well. Standard deviations were larger than the observed values for the majority (19) of the models, revealing either larger peaks or stronger fluctuations during the 24-month cycle.

With respect to moisture flux divergence (Fig. 4b), the picture is clearly different, with values distributed across much of the Taylor diagram as a result of clearly lower correlations and larger RMSD values compared to  $rENSO_i$ . Only one model (ACCESS-CM2) showed a correlation above 0.95 and RMSD below 0.4. The standard deviations ranged from 0.1 to 2.7 and were thus up to a factor of 2 larger than the observed value (1.3).

The multi-model mean aligns more closely with the observed mean than the individual models on average. Averaging the models thus cancels out biases in the individual models and the common signal inherent in the CMIP6 ensemble reasonably captures the key characteristics of the observed 24-month cycle.

### 3.3. Seasonal evolution of extreme and moderate El Niño events

The cycle (over two consecutive years) of an extreme El Niño event consists of a growth phase (slow warming) that peaks between November of the first year and January of the second year. This is followed by a decay phase (cooling) that lasts until at least the end of the second year. As revealed by Fig. 5a (left side), in the observational data the amplitude of this cycle during extreme El Niño events was much larger (maximum  $rENSO_i$  between 1.85 and 2.16 °C) than the corresponding amplitude during moderate El Niño events (average maximum  $rENSO_i$  1.13 °C; 10th percentile 0.88 °C, 90th percentile 1.25 °C). The data also indicated that during extreme El Niño events the asymmetry between slow warming and rapid cooling was more pronounced than during moderate El Niño events. Overall, the individual cycles of the four extreme El Niño events were comparable in terms of amplitude and timing, lying outside the range of cycles of the moderate events during the peak months.

Differences between extreme and moderate El Niño events cycles also emerged from the cycle of the moisture flux divergence, even more distinctly in this case (Fig. 5a, right side). During extreme El Niño events,  $\nabla \bullet \vec{Q}$ , which was positive at the beginning of the first year, rapidly shifted to negative values, attaining largest negative values (−2 to −5 mm day<sup>−1</sup>) in January of the second year. The phase characterized by negative values of  $\nabla \bullet \vec{Q}$  (i.e., moisture flux convergence or excess of

precipitation over evaporation) lasted for about 12 months, then changing to positive values of  $\nabla \bullet \vec{Q}$  only toward the end of the cycle (although with large differences in timing, among the individual extreme events). For most of the time, the evolution of  $\nabla \bullet \vec{Q}$  during extreme El Niño events was outside the range of moderate El Niño events, but for both the 1972–1973 as well as the 2015–2016 events the persistence of anomalous conditions ended as early as during the first half of the second year.

Concerning the representation of the evolution of extreme El Niño events in the models, Fig. 5b shows that the individual simulations captured the timing of the rENSOi fluctuations relatively well (gray lines in Fig. 5b, left panel). Furthermore, the magnitude of the extreme El Niño events varied considerably across the ensemble (Table 3). On average over the ensemble, the models matched the observed cycle remarkably well (dashed line in Fig. 5b as compared to the solid line). The same outcome was recorded for the moderate events (Fig. 5c, left).

Regarding moisture divergence the picture is noisier, with individual models showing varying temporal evolutions, magnitudes and timings of the peak (Fig. 5b and c, right panels and Table 4). For extreme El Niño events, the ensemble mean again followed the observed evolution very closely, whereas for the moderate events, there was a systematic difference between the observations and the models with large parts of the ensemble underestimating the observed values, particularly during the peak and decay phases of the cycle.

Fig. 6 presents another comparison of the model ensemble with the observed values for some key aspects of the seasonal cycle during extreme El Niño events. The timing of the peak month, although varying across individual members, was matched very well by the ensemble mean for both rENSOi and  $\nabla \bullet \vec{Q}$ . The magnitude of the rENSOi peak

was slightly overestimated by the CMIP6 ensemble, although the observed value (1.95 °C) was still within the 90% model range (1.1 °C–3.6 °C), indicating that the models identified more extreme Niño 3.4 SSTs than observations over the historical period. The middle panel of Fig. 6 illustrates the range between the largest and the smallest values across the identified extreme El Niño events. The CMIP6 ensemble reproduced the variability among rENSOi extremes well, but overestimated the differences between  $\nabla \bullet \vec{Q}$  amplitude among individual extreme events. Fig. S3 illustrates this for the individual models, many of which showed large negative peak values for some extreme events and almost no distinct peaks for others (e.g., GFDL-CM4).

The last two panels in Fig. 6 distinguish between moderate and extreme El Niño events. The fourth panel shows the number of months within the 24-month cycle, in which the average extreme events are outside the range of moderate events. This was the case for eleven months in the HadISST rENSOi dataset, a value exceeded by most model simulations, again indicating that the extreme SST events identified by CMIP6 tended to exceed those observed in magnitude. For  $\nabla \bullet \vec{Q}$  the difference between the observations and the models was even more striking, with all models underestimating the observed value. In ERA5, during 20 out of 24 months of the assessed cycle, the  $\nabla \bullet \vec{Q}$  values during extreme events were outside the range of the moderate events (Fig. 5a, right). The model interquartile range covered 9–14 months, demonstrating that in most simulations, moisture divergence was only extraordinary during the short period of the peaking phase, but indistinguishable from moderate events during the rest of the 24-month cycle (see Fig. S3). The last panel of Fig. 6 shows that whereas extreme event magnitude of rENSOi was overestimated by most models, this was not the case for moderate events, resulting in comparably large differences

**Table 3**

Comparison of the timing, maximum and minimum value of the relative ENSO index during extreme El Niño cycles as identified in the observations (HadISST; boldface) and each of the considered CMIP6 models. The mean values over the identified extreme events are shown, as well as the difference between simulated and observed values.

Dataset	Timing of the peak maximum value (peak)		Maximum		Minimum	
	Mean Month	Difference CMIP6 - Obs	Value	Difference CMIP6 - Obs	Value	Difference CMIP6 - Obs
<b>HadISST</b>	<b>12.3</b>		<b>2.0</b>		<b>-1.2</b>	
ACCESS-CM2	11.0	-1.3	2.0	0.0	-1.6	-0.4
ACCESS-ESM1-5	14.0	1.8	1.6	-0.4	-0.5	0.7
AWI-CM-1-1-MR	12.7	0.4	2.5	0.5	-1.3	0.0
BCC-CSM2-MR	10.0	-2.3	1.7	-0.2	-1.3	0.0
CAMS-CSM1-0	10.0	-2.3	2.3	0.3	-2.8	-1.6
CanESM5	12.3	0.1	1.7	-0.2	0.2	1.4
CESM2-WACCM	11.5	-0.8	3.6	1.6	-1.0	0.2
CESM2	12.0	-0.3	2.7	0.8	-1.6	-0.4
CIESM	12.3	0.1	2.3	0.4	-1.1	0.2
CMCC-ESM2	10.5	-1.8	3.6	1.7	-2.1	-0.8
CNRM-CM6-1-HR	12.3	0.1	1.1	-0.9	-0.6	0.7
CNRM-CM6-1	12.0	-0.3	2.6	0.7	-1.9	-0.7
CNRM-ESM2-1	12.0	-0.3	2.3	0.4	-2.4	-1.1
EC-Earth3-CC	12.3	0.1	2.0	0.1	-2.2	-0.9
FGOALS-f3-L	9.7	-2.6	2.2	0.3	-2.2	-0.9
FIO-ESM-2-0	11.5	-0.8	2.9	1.0	-1.6	-0.4
GFDL-CM4	11.0	-1.3	2.3	0.4	-1.0	0.2
GFDL-ESM4	11.5	-0.8	2.3	0.4	-1.9	-0.6
GISS-E2-1-G	8.7	-3.6	2.3	0.3	-0.7	0.6
HadGEM3-GC31-LL	10.0	-2.3	1.9	-0.1	-0.3	0.9
HadGEM3-GC31-MM	11.5	-0.8	1.8	-0.1	-1.7	-0.4
IITM-ESM	10.5	-1.8	1.8	-0.2	-1.8	-0.6
INM-CM5-0	10.0	-2.3	1.3	-0.7	-0.8	0.4
IPSL-CM6A-LR	12.0	-0.3	3.3	1.3	-1.2	0.0
MCM-UA-1-0	10.0	-2.3	2.0	0.0	-0.4	0.8
MIROC-ES2L	12.3	0.1	2.6	0.7	-1.5	-0.3
MIROC6	10.5	-1.8	2.9	1.0	-2.0	-0.7
MPI-ESM1-2-HR	16.0	3.8	1.7	-0.3	-0.1	1.2
MRI-ESM2-0	13.3	1.1	2.2	0.2	-0.9	0.4
NESM3	11.5	-0.8	2.1	0.1	-0.6	0.7
NorESM2-MM	11.5	-0.8	3.4	1.4	0.2	1.4
UKESM1-0-LL	12.3	0.1	2.3	0.4	-1.4	-0.1

**Table 4**  
Same as Table 3 but with respect to the spatially aggregated moisture flux divergence.

Dataset	Timing of the minimum value ("peak")		Minimum		Maximum	
	Mean Month	Difference CMIP6 - Obs	Value	Difference CMIP6 - Obs	Value	Difference CMIP6 - Obs
<b>ERA5</b>	<b>12.8</b>		<b>-3.9</b>		<b>1.1</b>	
ACCESS-CM2	12.0	-0.8	-5.2	-1.3	2.1	1.0
ACCESS-ESM1-5	9.7	-3.1	-2.9	1.0	1.4	0.3
AWI-CM-1-1-MR	12.3	-0.4	-4.0	0.0	0.5	-0.6
BCC-CSM2-MR	11.0	-1.8	-3.2	0.7	2.2	1.1
CAMS-CSM1-0	12.5	-0.3	-7.4	-3.4	2.0	0.9
CanESM5	13.3	0.6	-3.3	0.6	0.6	-0.5
CESM2-WACCM	13.0	0.3	-7.0	-3.1	0.8	-0.3
CESM2	13.0	0.3	-5.5	-1.6	1.6	0.5
CIESM	13.3	0.6	-4.5	-0.5	0.9	-0.3
CMCC-ESM2	12.0	-0.8	-6.2	-2.3	1.5	0.4
CNRM-CM6-1-HR	14.0	1.3	-2.3	1.6	0.9	-0.3
CNRM-CM6-1	13.5	0.8	-6.3	-2.4	2.0	0.9
CNRM-ESM2-1	13.3	0.6	-4.2	-0.3	1.4	0.3
EC-Earth3-CC	14.3	1.6	-5.4	-1.5	1.5	0.4
FGOALS-f3-L	11.7	-1.1	-6.3	-2.4	2.0	0.9
FIO-ESM-2-0	12.5	-0.3	-6.3	-2.4	1.6	0.5
GFDL-CM4	12.7	-0.1	-3.4	0.5	1.2	0.1
GFDL-ESM4	13.0	0.3	-3.9	0.1	0.9	-0.2
GISS-E2-1-G	12.3	-0.4	-6.8	-2.9	1.9	0.8
HadGEM3-GC31-LL	11.0	-1.8	-2.5	1.4	0.7	-0.4
HadGEM3-GC31-MM	12.5	-0.3	-5.2	-1.3	1.7	0.6
IITM-ESM	15.0	2.3	-4.5	-0.5	2.3	1.2
INM-CM5-0	9.7	-3.1	-1.6	2.3	1.0	-0.2
IPSL-CM6A-LR	13.5	0.8	-4.2	-0.3	1.2	0.1
MCM-UA-1-0	9.5	-3.3	-3.4	0.5	1.7	0.6
MIROC-ES2L	13.7	0.9	-5.3	-1.4	1.6	0.5
MIROC6	13.0	0.3	-6.3	-2.3	1.3	0.2
MPI-ESM1-2-HR	17.0	4.3	-2.0	1.9	1.2	0.1
MRI-ESM2-0	13.7	0.9	-6.7	-2.8	1.7	0.6
NESM3	13.5	0.8	-3.7	0.2	0.6	-0.5
NorESM2-MM	13.5	0.8	-5.9	-2.0	0.9	-0.2
UKESM1-0-LL	13.7	0.9	-4.4	-0.5	0.8	-0.3

between extreme and moderate peaks. For 90% of the simulations the observed 0.7 °C difference between moderate and extreme peaks was exceeded (mean of the models 1.2 °C). For  $\nabla \bullet \vec{Q}$  the smaller values in the simulations (-2.0 mm day<sup>-1</sup>) compared to ERA5 (-2.8 mm day<sup>-1</sup>) confirmed the limited ability of the CMIP6 ensemble to differentiate between moderate and extreme events in the atmospheric domain.

### 3.4. Spatial patterns of moisture flux divergence from extreme El Niño events

Fig. 7 shows the spatial patterns of  $\nabla \bullet \vec{Q}$  for extreme and moderate El Niño events in the observations and the CMIP6 ensemble mean. The observational record showed some clear differences between extreme and moderate events. Over the tropical Pacific, a distinct center of negative divergence (convergence) was established during extreme El Niño events around 170°W. The area characterized by magnitudes larger than 6 mm d<sup>-1</sup> extended over the Pacific as a broad branch ranging from 10°N to 5°S to the coasts of Ecuador and Peru. By contrast, during moderate events, the core of the negative divergence belt was located further west at 170°E (190°W) and the branch was much narrower (10°N to 5°N) and located further north, reaching the South American coast at the latitude of Colombia.

The CMIP6 models simulated the center of negative divergence during extreme El Niño events on average farther west (180°W), and the negative divergence branch over the Pacific is narrower and located farther north (10°N to 5°N) compared to the observations. By contrast, the average simulated patterns during moderate El Niño events were similar to the observed patterns. The spatial patterns confirmed the findings described earlier that the CMIP6 ensemble did not represent the differences in  $\nabla \bullet \vec{Q}$  between moderate and extreme El Niño events as neatly as did the observations. The individual mode simulations

(Fig. S4) were even more strongly different from the observations, often lacking the general pattern of convergence versus divergence manifested in ERA5.

## 4. Discussion

Due to our choice to identify extreme El Niño events based on a percentile threshold and given the length of the record, three such extremes were identified in HadISST (if only the time span between 1901 and 2014 is considered, with in addition 2015/2016) and two to three events were singled out in each of the CMIP6 models. Whereas in the observations all extreme events were clustered in the second half of the investigated period, extreme El Niño events were more evenly distributed along the time axis in many of the CMIP6 model records. This is not surprising. There is in fact emerging evidence that in the wake of changes in internal climate variability (Cai et al., 2021; Tang et al., 2020), ENSO dynamics underwent alterations over the course of the last century, with more central Pacific El Niño events occurring during the most recent decades than during the first half of the century (Freund et al., 2020). However, the mechanisms responsible for these shifts are not yet fully understood (Capotondi and Ricciardulli, 2021), which can explain the inability of global climate models to reproduce the observed transition.

Concerning the association between oceanic and atmospheric components in the ENSO system, the observations indicate a clear response of the latter to anomalous SST conditions during extreme El Niño events. The atmospheric moisture flux divergences in the area bounded by 170°W to 80°W in longitude and 8°N to 8°S in latitude, typically becomes negative as an El Niño cycle develops, and it does so more markedly during extreme El Niño events, resulting in peak negative values (about -4 mm day<sup>-1</sup>, on average) that are significantly more negative than observed during moderate El Niño events (-1 mm day<sup>-1</sup>).

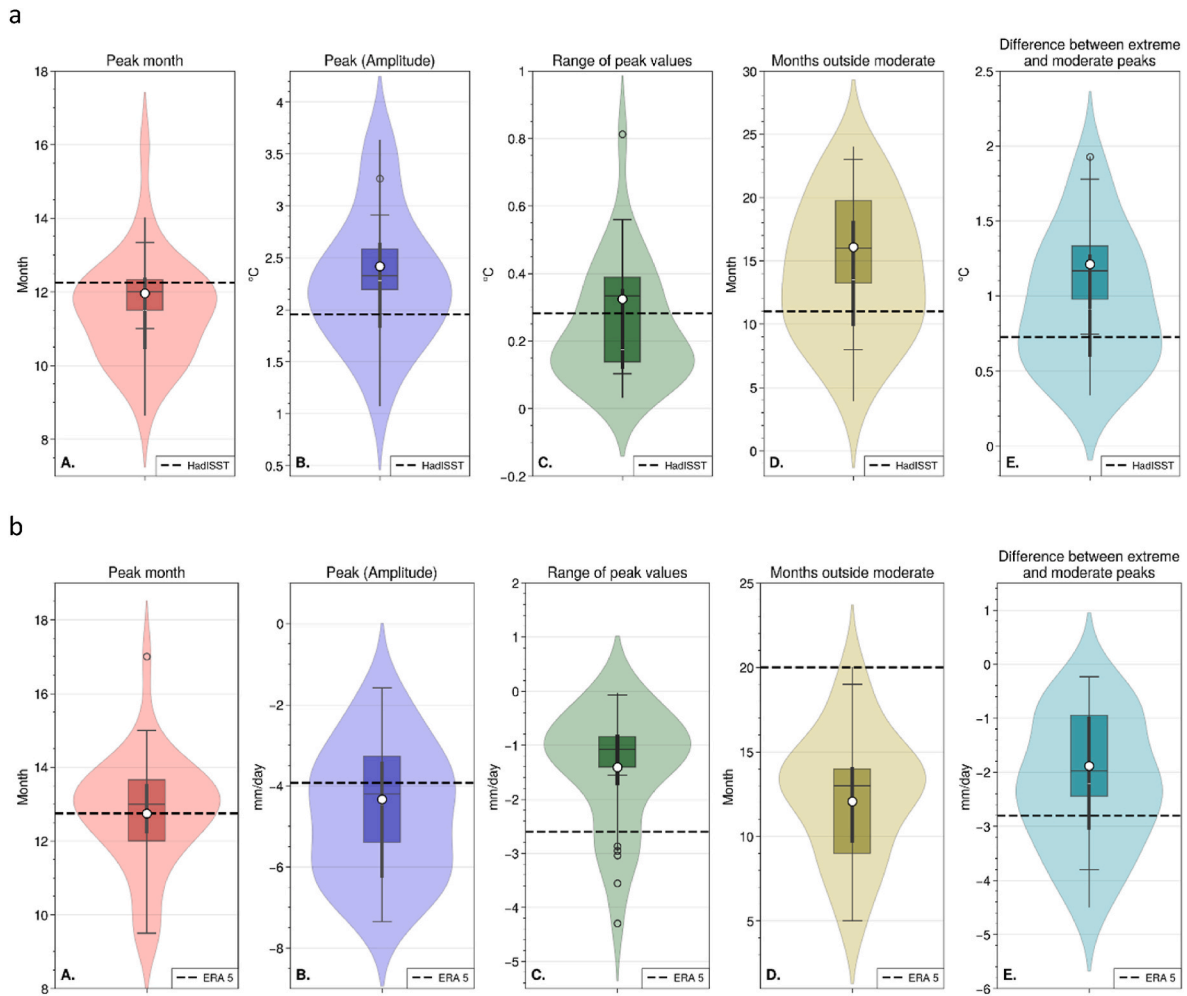


**Fig. 6.** Violin plots illustrating the statistical characteristics of the seasonal evolution of El Niño extreme events in observations and in the CMIP6 model ensemble for a) rENSOi and b) moisture flux divergence. From left to right: timing of the peak month, peak value (amplitude), difference in extreme peaks among the identified extreme events, number of months, where the average extreme events are outside the range of moderate events, and difference between extreme and moderate peaks. The observed values are indicated by the horizontal dashed lines, model ensemble averages are plotted as white dots. The box and whiskers plots inside the violin plots illustrate the median and the interquartile range of the distribution, the values extending the at most 1.5x the interquartile range, and the extrema. The outer contours of the violin plots illustrates the shape of the distribution of the seasonal evolution of the extreme El Niño events in the models.

The observational data further suggest a lag between the time of the rENSOi peak and the time of the most negative  $\nabla \bullet \vec{Q}$  of the order of one month. A number of examined CMIP6 models were able to capture this coupling between oceanic and atmospheric components and the corresponding time lag (extreme events with respect to rENSOi are also extreme with respect to  $\nabla \bullet \vec{Q}$ ). However, details of the coupling as simulated in the CMIP6 models often departed from the behavior disclosed by ERA5 and HadISST.

The different performance of the CMIP6 models with respect to the oceanic component (rENSOi), on the one hand, and the atmospheric component ( $\nabla \bullet \vec{Q}$ ), on the other hand, was evidenced by the Taylor diagrams (Fig. 4), even though in these diagrams the performance was only gauged in relation to the mean evolution of extreme El Niño events over a 24-month period. The lower performance in simulating the atmospheric component is underlined by lower values of the correlation coefficient and larger dispersion around the observational benchmark (larger RMSD) than for the case of the oceanic component. Similarly, the low ability of CMIP6 to reproduce the spatial patterns of divergence in El Niño extremes with anomaly centers farther west, less broad convergence branches and located farther north than the observed pattern resulted in inaccuracies in the seasonal evolution of convergence.

Models that did not exhibit significant differences between moderate

and extreme events in the seasonal cycle (time series of the extreme events mostly within the range of moderate events) also simulated spatial patterns that were almost identical for moderate and extreme events (ACCESS-ESM1-5, BCC-CSM2-MR, CanESM5, CNRM-CM6-1-HR, HadGEM3-GC31-LL, INM-CM5-0, and MPI-ESM1-2-HR). This lack of differentiation between moderate and extreme events usually featured a very weak seasonal cycle and very small divergence anomalies even during the peak season. Overall, the best performing model in our analysis was ACCESS-CM2, which captured the variance, timing and amplitude in the seasonal cycle of both rENSOi and  $\nabla \bullet \vec{Q}$  remarkably well and also reproduced the spatial patterns and associated differences between moderate and extreme events successfully.

Overestimation and underestimation of the amplitude of the  $\nabla \bullet \vec{Q}$  cycle in the CMIP6 ensemble may be attributed to the improper representation of the mechanisms linking surface fluxes to atmospheric moisture divergence (Peixoto and Oort, 1992; Trenberth et al., 2002). They could also be related to data processing and model parameterizations (He et al., 2022). The lack of adequate representation of the interaction between atmospheric forcing and oceanic processes may also be a contributing factor (Zhao and Karamperidou, 2022). Problems in the simulation of the oceanic component are likely associated with perturbations in the simulation of the ENSO blocking phase relative to

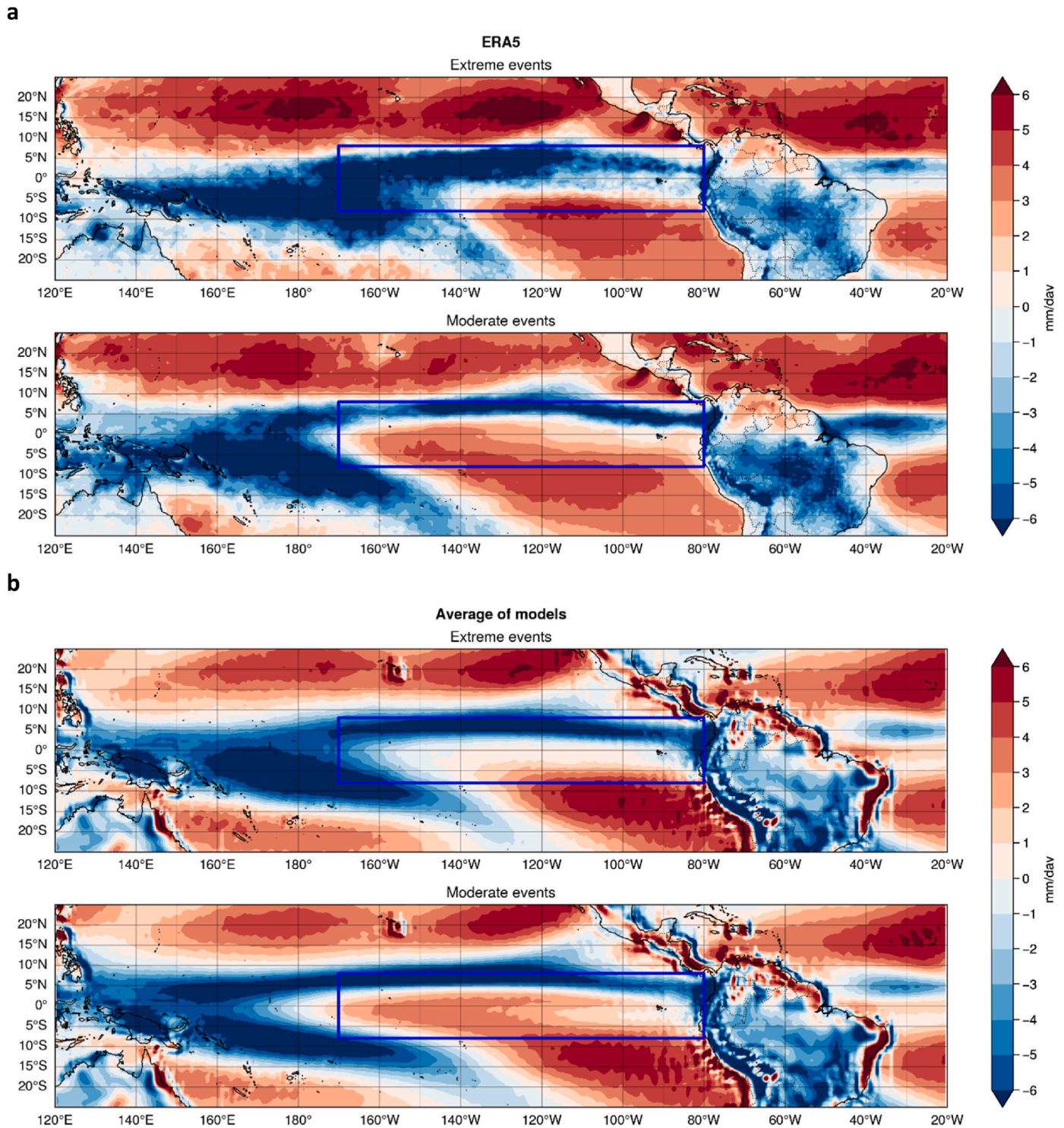


**Fig. 7.** Patterns of moisture flux divergence (convergence = negative divergence), mean for December to February (DJF), during extreme El Niño and moderate El Niño events. a) Observations; b) ensemble mean of the CMIP6 models.

the seasonal zonal SST cycle (Liao et al., 2021; Chen and Jin, 2022).

In addition to the aforementioned factors, the failure to accurately reproduce  $\nabla \cdot \vec{Q}$  patterns during extreme El Niño can be attributed to the inadequacy of climate models in representing modes of variability such as Pacific Meridional Modes (PMMs), the Pacific Decadal Oscillation (PDO), the Interdecadal Pacific Oscillation (IPO) (Jin, 2022), and modes of variability outside the Pacific (McKenna et al., 2020). As pointed out by Taschetto et al. (2020) inadequate representation of  $\nabla \cdot$

$\vec{Q}$  leads to the inability to accurately depict rainfall teleconnections.

### 5. Conclusions

The recent decade has witnessed important advances in relation to seasonal ENSO outlooks (e.g., L'Heureux et al., 2017; 2019). This means that once ENSO is in a given phase, the current GCMs are able to simulate its further evolution. Improvements in seasonal predictions

have been possible due to a better understanding and formulation of the processes governing oceanic variability and its coupling with atmospheric dynamics, as well as the adoption of new techniques, such as the application of deep learning (Patil et al., 2022). Nevertheless, much remains to be done to advance climate simulations of ENSO in settings where model runs are initialized without incorporating data assimilation, as in seasonal forecasting. This is especially true for the occurrence of extreme El Niño events and the associated links to atmospheric circulation. In this paper, we have examined a 32-member ensemble of CMIP6 models. On average, the model ensemble captured the magnitude and timing of the seasonal evolution during extreme El Niño events remarkably well, at least in relation to the oceanic and atmospheric indices considered here. With a few exceptions, variations in RENS0i and differences in moderate events were also reasonably depicted by the individual model simulations. By contrast, many models failed to reasonably reproduce the clear distinction between moderate and extreme events in the observed atmospheric moisture flux dynamics over the tropical Pacific. This suggests the limited capabilities of the examined climate models to reasonably predict the hydrological consequences of extreme tropical Pacific SSTs in South America and other regions affected by ENSO teleconnections.

The deficiencies disclosed by our work are well supported by the results of other studies (Song et al., 2020; Liao et al., 2021; Planton et al., 2021; Geng et al., 2023; De Silva et al., 2023). Our findings lend to the conclusion that many of the current GCMs, even if capable of capturing the oceanic flavor of extreme El Niño events, do not yet provide a reliable starting point for investigating the impacts of such events on regional atmospheric dynamics and precipitation in tropical South America. As pointed out by Cai et al. (2020) and Sanabria et al. (2018, 2019), these atmospheric and hydrological responses to extreme El Niño events are not always the same, exhibiting variations from event to event.

The frequency of extreme El Niño events is expected to increase in the future (Cai et al., 2014, 2017; Wang et al., 2017). In addition, ENSO teleconnection patterns may continue to change in the future (McGregor et al., 2022; Alizadeh, 2024; Lieber et al., 2024), as they did in the past (Dätwyler et al., 2019; Luo et al., 2022; Han et al., 2023). As in many cases the assessment of future teleconnection changes is based on the climate models considered in this study, with their limitations in simulating atmospheric responses to SST extremes. Thus caution is required in interpreting both the temporal and spatial patterns of simulated regional and large-scale dynamic responses to ENSO extreme events in impact assessments. This is particularly true if only individual models are assessed. Although it is beyond the scope of the present investigation to address ENSO dynamics, future modeling efforts may prioritize the dynamic response of the tropical troposphere to improve the models' capabilities in capturing spatiotemporal patterns during extreme El Niño events.

#### CRediT authorship contribution statement

**Janeet Sanabria:** Writing – review & editing, Writing – original draft, Validation, Software, Investigation, Formal analysis, Conceptualization. **Raphael Neukom:** Writing – review & editing, Writing – original draft, Conceptualization. **Alan Llacza:** Software. **Nadine Salzmann:** Writing – review & editing, Writing – original draft. **Pierluigi Calanca:** Writing – review & editing, Writing – original draft, Methodology, Conceptualization.

#### Declaration of competing interest

The authors declare the following financial interests/personal relationships which may be considered as potential competing interests: Janeet Sanabria reports financial support was provided by Swiss confederation - Swiss Government Excellence Scholarships. Janeet Sanabria reports a relationship with Swiss Confederation - Swiss

Government Excellence Scholarships that includes: funding grants. If there are other authors, they declare that they have no known competing financial interests or personal relationships that could have appeared to influence the work reported in this paper.

#### Acknowledgments, Samples, and Data

Met-Office Hadley Centre HadISST data (<https://www.metoffice.gov.uk/hadobs/hadisst/data/download.html>). CMIP6 Data of The Institute for Atmospheric and Climate Science (IAC) of the Swiss Federal Institute of Technology Zurich (ETH Zurich) <https://data.iac.ethz.ch/atmos/net/atmos/data/cmip6>. ECMWF ERA5 data <https://cds.climate.copernicus.eu/cdsapp#!/dataset/reanalysis-era5-complete?tab=form>. This research was funded by Swiss Government Excellence Scholarships selected.

#### Appendix A. Supplementary data

Supplementary data to this article can be found online at <https://doi.org/10.1016/j.wace.2025.100746>.

#### Data availability

Data will be made available on request.

#### References

- Alizadeh, O., 2024. A review of ENSO teleconnections at present and under future global warming. *WIREs Climate Change* 15 (1), e861. <https://doi.org/10.1002/wcc.861>.
- Balaji, V., Taylor, K.E., Jukes, M., Lawrence, B.N., Durack, P.J., Lautenschlager, M., Blanton, C., Cinquini, L., Denvil, S., Elkington, M., Guglielmo, F., Guilyardi, E., Hassell, D., Kharin, S., Kindermann, S., Nikonov, S., Radhakrishnan, A., Stockhouse, M., Weigel, T., Williams, D., 2018. Requirements for a global data infrastructure in support of CMIP6. *Geosci. Model Dev. (GMD)* 11, 3659–3680. <https://doi.org/10.5194/gmd-11-3659-2018>.
- Battisti, D.S., Hirst, A.C., 1989. Interannual variability in the tropical atmosphere-ocean model: influence of the basic state, ocean geometry and nonlinearity. *J. Atmos. Sci.* 46 (2), 1687–1712. [https://doi.org/10.1175/1520-0469\(1989\)046%3C1687:IVIATA%3E2.0.CO](https://doi.org/10.1175/1520-0469(1989)046%3C1687:IVIATA%3E2.0.CO).
- Bell, B., Hersbach, H., Simmons, A., Berrisford, P., Dahlgren, P., Horányi, A., et al., 2021. The ERA5 global reanalysis: preliminary extension to 1950. *Q. J. R. Meteorol. Soc.* 147 (741), 4186–4227. <https://doi.org/10.1002/qj.4174>.
- Bjerknes, J.A., 1966. Possible response of the atmospheric Hadley Circulation to equatorial anomalies of ocean temperature. *Tellus* 4, 820–829. <https://doi.org/10.1111/j.2153-3490.1966.tb00303.x>.
- Bjerknes, J.A., 1969. Atmospheric teleconnections from the equatorial Pacific. *Mon. Weather Rev.* 97 (2), 163–172. [https://doi.org/10.1175/1520-0493\(1969\)097<0163:ATFTEP>2.3.CO](https://doi.org/10.1175/1520-0493(1969)097<0163:ATFTEP>2.3.CO).
- Boers, N., Donner, R.V., Bookhagen, B., Kurths, J., 2014. Complex network analysis helps to identify impacts of the El Niño Southern Oscillation on moisture divergence in South America. *Clim. Dyn.* <https://doi.org/10.1007/s00382-014-2265-7>.
- Cai, W., Borlace, S., Lengaigne, M., van Rensch, P., Collins, M., Vecchi, B., Timmermann, A., Santoso, A., McPhaden, M.J., Wu, L., England, M.H., Wang, G., Guilyardi, E., Jin, F.-F., 2014. Increasing frequency of extreme El Niño events due to greenhouse warming. *Nat. Clim. Change* 4, 111–116. <https://doi.org/10.1038/nclimate2100>.
- Cai, W., Wang, G., Santoso, A., et al., 2015. Increased frequency of extreme La Niña events under greenhouse warming. *Nat. Clim. Change* 5, 132–137. <https://doi.org/10.1038/nclimate2492>.
- Cai, W., Wang, G., Santoso, A., Lin, X., Wu, L., 2017. Definition of extreme El Niño and its impact on projected increase in extreme El Niño frequency. *Geophys. Res. Lett.* 44. <https://doi.org/10.1002/2017GL075635>, 11 184–11 190.
- Cai, W., McPhaden, M.J., Grimm, A.M., Rodrigues, R.R., Taschetto, A.S., Garreaud, R.D., Dewitte, B., Poveda, G., Ham, Y.-G., Santoso, A., Ng, B., Anderson, W., Wang, G., Geng, T., Jo, H.-S., Marengo, J.A., Alves, L.M., Osman, M., Li, S., Wu, L., Karamperidou, C., Takahashi, K., Vera, C., 2020. Climate impacts of the el niño-southern oscillation on South America. *Nat. Rev. Earth Environ.* 1, 215–231. <https://doi.org/10.1038/s43017-020-0040-3>.
- Cai, W., Santoso, A., Collins, M., Dewitte, B., Karamperidou, C., Kug, J.-S., Lengaigne, M., McPhaden, M.J., Stuecker, M.F., Taschetto, A.S., Timmermann, A., Wu, L., Yeh, S.-W., Wang, G., Ng, B., Jia, F., Yang, Y., Ying, J., Zheng, X.-T., Bayr, T., Brown, J.R., Capotondi, A., Cobb, K.M., Gan, B., Geng, T., Ham, Y.-G., Jin, F.-F., Jo, H.-S., Li, X., Lin, X., McGregor, S., Park, J.-H., Stein, K., Yang, K., Zhang, L., Zhong, W., 2021. Changing el niño-southern oscillation in a warming climate. *Nat. Rev. Earth Environ.* 2, 628–644. <https://doi.org/10.1038/s43017-021-00199-z>.
- Capotondi, A., Coauthors, 2015. Understanding ENSO diversity. *Bull. Am. Meteorol. Soc.* 96, 921–938. <https://doi.org/10.1175/BAMS-D-13-00117.1>.

- Capotondi, A., Ricciardulli, L., 2021. The influence of Pacific winds on ENSO diversity. *Sci. Rep.* 11, 18672. <https://doi.org/10.1038/s41598-021-97963-4>.
- Chen, L., Li, T., Wang, B., Wang, L., 2017. Formation mechanism for 2015/16 super El Niño. *Sci. Rep.* 7, 2975. <https://doi.org/10.1038/s41598-017-02926-3>.
- Chen, H.-C., Jin, F.-F., 2022. Dynamics of ENSO phase-locking and its biases in climate models. *Geophys. Res. Lett.* 49, e2021GL097603. <https://doi.org/10.1029/2021GL097603>.
- Davey, M.K., Brookshaw, A., Ineson, S., 2014. The probability of the impact of ENSO on precipitation and near-surface temperature. *Clim. Risk Manag.* 1, 5–24. <https://doi.org/10.1016/j.crm.2013.12.002>.
- Dätwyler, C., Abram, N.J., Grosjean, M., Wahl, E.R., Neukom, R., 2019. ENSO variability, teleconnection changes and responses to large volcanic eruptions since AD 1000. *Int. J. Climatol.* 39 (ja), 2711–2724. <https://doi.org/10.1002/joc.5983>.
- De Silva, Y.K., Babel, M.S., Abatan, A.A., Khadka, D., Shanmugasundaram, J., 2023. Evaluation of ENSO in CMIP5 and CMIP6 models and its significance in the rainfall in Northeast Thailand. *Theor. Appl. Climatol.* <https://doi.org/10.1007/s00704-023-04585-z>.
- Dewitte, B., Takahashi, K., 2019. Extreme El Niño events. In: Venugopal, V., Sukhatme, J., Murtugudde, R., Roca, R. (Eds.), *Tropical Extremes: Natural Variability and Trends*. Elsevier, Amsterdam, pp. 165–201. <https://doi.org/10.1016/B978-0-12-809248-4.00006-6>.
- Eyring, V., Bony, S., Meehl, G.A., Senior, C.A., Stevens, B., Taylor, Stouffer R.J., 2016. Overview of the coupled model Intercomparison Project phase 6 (CMIP6) experimental design and organization. *Geosci. Model Dev. (GMD)* 9, 1937–1958. <https://doi.org/10.5194/gmd-9-1937-2016>.
- Freund, M.B., Brown, J.R., Henley, B.J., Karoly, D.J., Brown, J.N., 2020. Warming patterns affect El Niño diversity in CMIP5 and CMIP6 models. *J. Clim.* 33, 8237–8260. <https://doi.org/10.1175/JCLI-D-19-0890.1>.
- Geng, T., Jia, F., Cai, W., Wu, L., Bolan, G., Jing, Z., Li, S., McPhaden, M.J., 2023. Increased occurrences of consecutive La Niña events under global warming. *Nature* 619, 774–781. <https://doi.org/10.1038/s41586-023-06236-9>.
- Guilyardi, E., Bellenger, H., Collins, M., Ferret, S., Cai, W., Wittenberg, A., 2012. A first look at ENSO in CMIP5. *Clivar Exchanges* 17 (58), 29–32. <https://www.clivar.org/sites/default/files/documents/Exchanges58.pdf>.
- Hameed, S.N., Jin, D., Thilakan, V.A., 2018. Model for super el Niños. *Nat. Commun.* 9, 2528. <https://doi.org/10.1038/s41467-018-04803-7>.
- Han, X., Li, Y., Liu, F., Li, J., Zheng, X., Li, Y., Feng, L., 2023. Stability of ENSO teleconnections during the last millennium in CESM. *Clim. Dyn.* 61 (11), 5699–5714. <https://doi.org/10.1007/s00382-023-06878-5>.
- He, J., Brogniez, H., Picon, L., 2022. Evaluation of tropical water vapour from CMIP6 global climate models using the ESA CCI Water Vapour climate data records. *Atmos. Chem. Phys.* 22, 12591–12606. <https://doi.org/10.5194/acp-22-12591-2022>.
- Hoerling, M.P., Kumar, A., Zhong, M., 1997. El Niño, La Niña, and the nonlinearity of their teleconnections. *J. Clim.* 10, 1769–1786. [https://doi.org/10.1175/1520-0442\(1997\)010<1769:ENOLNA>2.0.CO;2](https://doi.org/10.1175/1520-0442(1997)010<1769:ENOLNA>2.0.CO;2).
- Hong, L.-C., LinHo, Jin, F.-F., 2014. A southern hemisphere booster of super El Niño. *Geophys. Res. Lett.* 41, 2142–2149. <https://doi.org/10.1002/2014GL059370>.
- Hou, M., Tang, Y., 2022. Recent progress in simulating two types of ENSO— from CMIP5 to CMIP6. *Front. Mar. Sci.* 9, 986780. <https://doi.org/10.3389/fmars.2022.986780>.
- Humanez-Fuente, V., Ferrero, M.E., Muñoz, A.A., González-Reyes, Á., Requena-Rojas, E. J., Barichivich, J., et al., 2020. Two centuries of hydroclimatic variability reconstructed from tree-ring records over the Amazonian Andes of Peru. *J. Geophys. Res. Atmos.* 125, e2020JD032565. <https://doi.org/10.1029/2020JD032565>.
- Jin, F.-F., 2022. Toward understanding el Niño southern-oscillation's spatiotemporal pattern diversity. *Front. Earth Sci.* 10, 899139. <https://doi.org/10.3389/feart.2022.899139>.
- Johnson, N.C., Kosaka, Y., 2016. The impact of eastern equatorial Pacific convection on the diversity of boreal winter El Niño teleconnection patterns. *Clim. Dyn.* 47, 3737–3765. <https://doi.org/10.1007/s00382-016-3039-1>.
- Kiladis, G.N., Diaz, H.F., 1989. Global climatic anomalies associated with extremes in the southern oscillation. *J. Clim.* 2, 1069–1090. [https://doi.org/10.1175/1520-0442\(1989\)002<1069:GCAAWE>2.0.CO;2](https://doi.org/10.1175/1520-0442(1989)002<1069:GCAAWE>2.0.CO;2).
- Kim, W., Cai, W., Kug, J.-S., 2015. Migration of atmospheric convection coupled with ocean currents pushes el Niño to extremes. *Geophys. Res. Lett.* 42, 3583–3590. <https://doi.org/10.1002/2015GL063886>.
- King, M.P., Yu, E.T., Sillmann, J., 2020. Impact of strong and extreme El Niños on European hydroclimate. *Tellus Dyn. Meteorol. Oceanogr.* 72 (1), 1–10. <https://doi.org/10.1080/16000870.2019.1704342>.
- Larkin, N.K., Harrison, D.E., 2002. ENSO warm (El Niño) and cold (La Niña) event life cycles: ocean surface anomaly patterns, their symmetries, asymmetries, and implications. *J. Clim.* 15, 1118–1140. [https://doi.org/10.1175/1520-0442\(2002\)015<1118:EWENOA>2.0.CO;2](https://doi.org/10.1175/1520-0442(2002)015<1118:EWENOA>2.0.CO;2).
- L'Heureux, M.L., Takahashi, K., Watkins, A.B., Barnston, A.G., Becker, E.J., Di Liberto, T. E., Gamble, F., Gottschalck, J., Halpert, M.S., Huang, B., Mosquera-Vásquez, K., Wittenberg, A.T., 2017. Observing and predicting the 2015/16 el Niño. *Bull. Am. Meteorol. Soc.* 98 (7), 1363–1382. <https://doi.org/10.1175/BAMS-D-16-0009.1>.
- L'Heureux, M.L., Tippet, M.K., Takahashi, K., Barnston, A.G., Becker, E.J., Bell, G.D., Di Liberto, T.E., Gottschalck, J., Halpert, M.S., Hu, Z., Johnson, N.C., Xue, Y., Wang, W., 2019. Strength outlooks for the el Niño—southern oscillation. *Weather Forecast.* 34 (1), 165–175. <https://doi.org/10.1175/WAF-D-18-0126.1>.
- L'Heureux, M.L., Tippet, M.K., Wheeler, M.C., Nguyen, H., Narsey, S., Johnson, N., Hu, Z.-Z., Watkins, A.B., Lucas, C., Ganter, C., Becker, E., Wang, W., Di Liberto, T., 2024. A relative Sea Surface Temperature Index for classifying ENSO events in a changing climate. *J. Clim.* 37, 1197–1211. <https://doi.org/10.1175/JCLI-D-23-0406.1>.
- Lieber, R., Brown, J., King, A., Freund, M., 2024. Historical and future asymmetry of ENSO teleconnections with extremes. *J. Clim.* 37 (22), 5909–5924. <https://doi.org/10.1175/JCLI-D-23-0619.1>.
- Latif, M., Keenlyside, N.S., 2009. El Niño/Southern Oscillation response to global warming. *Proc. Natl. Acad. Sci. USA* 106 (49), 20578–20583. <https://doi.org/10.1073/pnas.0710860105>.
- Lengaigne, M., Vecchi, G.A., 2010. Contrasting the termination of moderate and extreme El Niño events in coupled general circulation models. *Clim. Dyn.* 35, 299–313. <https://doi.org/10.1007/s00382-009-0562-3>.
- Liao, H., Wang, C., Song, Z., 2021. ENSO phase-locking biases from the CMIP5 to CMIP6 models and a possible explanation. *Deep Sea Res. Part II: Top. Stud. Oceanogr.* 2, 189–190. <https://doi.org/10.1016/j.dsr2.2021.104943>.
- Luo, X., Dee, S., Stevenson, S., Okumura, Y., Steiger, N., Parsons, L., 2022. Last millennium ENSO diversity and north American teleconnections: new insights from paleoclimate data assimilation. *Paleoceanogr. Paleoclimatol.* 37 (3), e2021PA004283. <https://doi.org/10.1029/2021PA004283>.
- McGregor, S., Cassou, C., Kosaka, Y., Phillips, A.S., 2022. Projected ENSO teleconnection changes in CMIP6. *Geophys. Res. Lett.* 49, e2021GL097511. <https://doi.org/10.1029/2021GL097511>.
- McKenna, S., Santoso, A., Gupta, A.S., Taschetto, A.S., Cai, W., 2020. Indian Ocean Dipole in CMIP5 and CMIP6. characteristics, biases, and links to ENSO. *Sci. Rep.* 10, 1150. <https://doi.org/10.1038/s41598-020-68268-9>.
- Neelin, J.D., Battisti, D.S., Hirst, A.C., Jin, F.-F., Wakata, Y., Yamagata, T., Zebiak, S.E., 1998. ENSO theory. *J. Geophys. Res.* 103. <https://doi.org/10.1029/97JC03424>, 14 261–14 290.
- Oldenborgh, V., Geert, J., Hendon, H., Stockdale, T., L'Heureux, M., Coughlan de Perez, E., Singh, R., van Aalst, M., 2021. Defining El Niño indices in a warming climate. *Environ. Res. Lett.* 16, 044003. <https://iopscience.iop.org/article/10.1088/1748-9326/abe9ed>.
- Patil, K.R., Doi, T., Jayanthi, V.R., Behera, S., 2022. Deep learning for skillful long-lead ENSO forecasts. *Front. Clim.* 4, 1058677. <https://doi.org/10.3389/fclim.2022.1058677>.
- Paixao Veiga, J.A., Rao, V.B., Franchito, S.H., 2005. Heat and moisture budgets of the walker circulation and associated rainfall anomalies during El Niño events. *Int. J. Climatol.* 25, 193–213. <https://doi.org/10.1002/joc.1115>.
- Peixoto, J.P., Oort, A.H., 1992. *Physics of Climate*. American Institute of Physics, MIT press, San Diego, CA, p. 520.
- Planton, Y.Y., Guilyardi, E., Wittenberg, A.T., Lee, J., Gleckler, P.J., Bayr, T., McGregor, S., McPhaden, M.J., Power, S., Roehrig, R., Vialard, J., Voldoire, A., 2021. Evaluating climate models with the CLIVAR 2021 ENSO metrics package. *Bull. Am. Meteorol. Soc.* 102, E193–E217. <https://doi.org/10.1175/BAMS-D-19-0337.1>.
- Rasmusson, E.M., Carpenter, T.H., 1982. Variations in tropical sea surface temperature and surface wind fields associated with the Southern Oscillation/El Niño. *Mon. Weather Rev.* 110, 354–384. [https://doi.org/10.1175/1520-0493\(1982\)110<0354:VITSST>2.0.CO;2](https://doi.org/10.1175/1520-0493(1982)110<0354:VITSST>2.0.CO;2).
- Rayner, N.A., Parker, D.E., Horton, E.B., Folland, C.K., Alexander, L.V., Rowell, D.P., Kent, E.C., Kaplan, A., 2003. Global analyses of sea surface temperature, sea ice, and night marine air temperature since the late nineteenth century. *Geophys Res Lett.* 30, 1–20. <https://doi.org/10.1029/2002JD002670>.
- Ropelewski, C.H., Halpert, S., 1987. Global and regional scale precipitation patterns associated with the El Niño/Southern Oscillation. *Mon. Weather Rev.* 115 (2), 1606–1626. [https://doi.org/10.1175/1520-0493\(1987\)115<1606:GARSPP>2.0.CO](https://doi.org/10.1175/1520-0493(1987)115<1606:GARSPP>2.0.CO).
- Sanabria, J., Bourrel, L., Dewitte, B., Frappart, F., Rau, P., Solis, O., Labat, D., 2018. Rainfall along the coast of Peru during strong El Niño events. *Int. J. Climatol.* 38, 1737–1747. <https://doi.org/10.1002/joc.5292>.
- Sanabria, J., Carrillo, C.M., Labat, D., 2019. Unprecedented rainfall and moisture patterns during el Niño 2016 in the eastern Pacific and tropical Andes: northern Peru and Ecuador. *Atmosphere* 10, 768. <https://doi.org/10.3390/atmos10120768>, 2019.
- Santoso, A., McPhaden, M.J., Cai, W., 2017. The defining characteristics of ENSO extremes and the strong 2015/2016 El Niño. *Rev. Geophys.* 55, 1079–1129. <https://doi.org/10.1002/2017RG000560>.
- Song, Z., Liu, H., Chen, X., 2020. Eastern Equatorial Pacific SST seasonal cycle in global climate models: from CMIP5 to CMIP6. *Acta Oceanol. Sin.* 39, 50–60. <https://doi.org/10.1007/s13131-020-1623-z>.
- Sulca, J., Takahashi, K., Espinoza, J.-C., Vuille, M., Lavado-Casimiro, W., 2018. Impacts of different ENSO flavors and tropical Pacific convection variability (ITCZ, SPCZ) on austral summer rainfall in South America, with a focus on Peru. *Int. J. Climatol.* 38, 420–435. <https://doi.org/10.1002/joc.5185>.
- Takahashi, K., Montecinos, A., Goubanova, K., Dewitte, B., 2011. ENSO regimes: reinterpreting the canonical and Modoki El Niño. *Geophys. Res. Lett.* 38, L10704. <https://doi.org/10.1029/2011GL047364>.
- Tang, S., von Storch, H., Chen, X., 2020. Atmospherically forced regional ocean simulations of the South China sea: scale dependency of the signal-to-noise ratio. *J. Phys. Oceanogr.* 50, 133–144. <https://doi.org/10.1175/JPO-D-19-0144.1>.
- Taschetto, A.S., Ummerhofer, C.C., Stuecker, M.F., Dommengat, D., Ashok, K., Rodrigues, R.R., Yeh, S.-W., 2020. ENSO atmospheric teleconnections, El Niño Southern Oscillation in a changing climate, 309–335. <https://doi.org/10.1002/9781119548164.ch14>.
- Trenberth, K.E., Caron, J.M., Stepaniak, D.P., Worley, S., 2002. Evolution of el Niño—southern oscillation and global atmospheric surface temperatures. *J. Geophys. Res.* 107. <https://doi.org/10.1029/2000JD000298>. AAC 5-1-AAC 5-17.
- Trenberth, K.E., 2020. ENSO in the global climate system. In: McPhaden, M.J., Santoso, A., Cai, W. (Eds.), *El Niño Southern Oscillation in a Changing Climate*. Geophysical Monographs Series, American Geophysical Union, Boston, pp. 21–37.

- <https://doi.org/10.1002/9781119548164>. <https://agupubs.onlinelibrary.wiley.com/doi/book/10.1002/9781119548164>.
- Thielen, D.R., Ramoni-Perazzi, P., Zamora-Ledezma, E., Puche, M.L., Marquez, M., Quintero, J.I., Rojas, W., Quintero, A., Bianchi, G., Soto-Werschitz, I.A., Arizapana-Almonacid, M.A., 2023. Effect of extreme El Niño events on the precipitation of Ecuador. *Nat. Hazards Earth Syst. Sci.* 23, 1507–1527. <https://doi.org/10.5194/nhess-23-1507-2023>.
- Vimont, D.J., Newman, M., Battisti, D.S., Shin, S.-I., 2022. The role of seasonality and the ENSO mode in central and east pacific ENSO growth and evolution. *J. Clim.* 1, 1–46. <https://doi.org/10.1175/JCLI-D-21-0599.1>.
- Wallace, J.M., Rasmusson, E.M., Mitchell, T.P., Kousky, V.E., Sarachik, E.S., 1998. On the structure and evolution of ENSO-related climate variability in the tropical Pacific: lessons from TOGA. *J. Geophys. Res.* 103. <https://doi.org/10.1029/97JC02905>, 14 241–14 259.
- Wang, C., 2000. On the atmospheric responses to tropical pacific heating during the mature phase of el Niño. *J. Atmos. Sci.* 57, 3767–3781. [https://doi.org/10.1175/1520-0469\(2000\)057<3767:OTARTT>2.0.CO;2](https://doi.org/10.1175/1520-0469(2000)057<3767:OTARTT>2.0.CO;2).
- Wang, G., Cai, W., Gan, B., Wu, L., Santoso, A., Lin, X., Chen, Z., McPhaden, M.J., 2017. Continued increase of extreme El Niño frequency long after 1.5 C warming stabilization. *Nat. Clim. Change* 7, 568–572. <https://doi.org/10.1038/nclimate3351>.
- Watterson, I.G., Keane, R.J., Dix, M., Ziehn, T., Andrews, T., Tang, Y., 2021. Analysis of CMIP6 atmospheric moisture fluxes and the implications for projections of future change in mean and heavy rainfall. *Int. J. Climatol.* 41 (Suppl. 1), E1417–E1434. <https://doi.org/10.1002/joc.6777>.
- Xu, G., Osborn, T.J., Matthews, A.J., Joshi, M.M., 2015. Different atmospheric moisture divergence responses to extreme and moderate El Niño. *Clim. Dyn.* 47, 393–410. <https://doi.org/10.1007/s00382-015-2844-2>.
- Yu, J.-Y., Kim, S.-T., 2013. Identifying the types of major El Niño events since 1870. *Int. J. Climatol.* 33 (8), 2105–2112. <https://doi.org/10.1002/joc.3575>.
- Zhao, S., Karamperidou, C., 2022. Competing effects of eastern and central-western Pacific winds in the evolution of the 2017 extreme coastal El Niño. *Geophys. Res. Lett.* 49, e2022GL098859. <https://doi.org/10.1029/2022GL098859>.